Analytical Inverse Design of GRIN Lens Antennas: The Phase Tracing Method

Gashi, I., Maci, S., Albani, M. (2026). Analytical Inverse Design of GRIN Lens Antennas: The Phase Tracing Method. IEEE TRANSACTIONS ON ANTENNAS AND PROPAGATION, 1-1 [10.1109/tap.2026.3676548].

DOI: http://doi.org/10.1109/tap.2026.3676548

This article has been accepted for publication in IEEE Transactions on Antennas and Propagation. This is the author's version which has not been fully edited and content may change prior to final publication. Citation information: DOI 10.1109/TAP.2026.3676548

Analytical Inverse Design of GRIN Lens Antennas: The Phase Tracing Method

Ilir Gashi, *Member, IEEE*, Stefano Maci, *Fellow, IEEE*, and Matteo Albani, *Fellow, IEEE*

***Abstract*—This paper presents the phase tracing method (PTM), an analytical framework for the direct synthesis of graded-index (GRIN) lens antennas. PTM employs an inverse formulation of geometrical optics (GO) principles to derive isotropic refractive index profiles directly from user-specified ray trajectories. By circumventing the computational expense and convergence challenges of numerical optimization, and relaxing the constraints of classical analytical approaches, PTM enables deterministic control over both phase and amplitude transformations at the aperture. Its core innovation lies in establishing explicit relationships between ray curvature, phase evolution, and refractive index gradients under strict power conservation, allowing for analytically tractable designs. The method further leverages clothoid trajectories, characterized by linearly varying curvature, to produce smooth, bounded refractive index gradients conducive to fabrication. The versatility of PTM is demonstrated through five examples: (a) exact analytical retrieval of the Maxwell Fish-Eye lens, (b) a telescopic GRIN lens achieving 2× aperture magnification, (c) a flat-top beam generator with uniform ±15° coverage, (d) a Bessel beam launcher for non-diffracting radiation, and (e) a GRIN lens transforming a rectangular waveguide mode into a uniform circular aperture. The designs are validated via full-wave simulations, GO analysis, and theoretical benchmarks, confirming exceptional performance. PTM establishes a new paradigm for efficient, wideband GRIN lens design, combining analytical rigor with practical manufacturability for microwave and millimeter-wave applications.**

***Index Terms*—Inhomogeneous lenses, GRIN media, Geometrical Optics, Phase Tracing Method, Inverse Design, Lens Synthesis.**

I. INTRODUCTION

Graded-index (GRIN) lens antennas offer key advantages over conventional lenses, particularly in enabling flat interfaces with free space and allowing control of both amplitude and phase across an aperture over ultra-wide bandwidths. The rays follow arbitrary curved paths inside the lens because they are smoothly and continuously bent by the refractive index gradient. Therefore, the use of geometrical optics (GO) [1], [2], [3] for inhomogeneous media finds its natural application in this class of problems. The analysis problem can be performed by tracing the rays [4] or by employing a faster numerical approach—the Lax–Friedrichs sweeping method, which we have recently introduced in [5]. This method iteratively and efficiently solves fundamental GO equations with higher accuracy compared to traditional ray tracing, making it particularly suitable for integration within optimization-based design frameworks.

However, the practical realization of GRIN lenses has long been constrained by manufacturing challenges. Traditional implementations often require discretization into concentric shells, which introduces scattering losses and degrades performance. Recent technological advances have significantly increased the feasibility of fabricating GRIN lenses, stimulating renewed research interest. Additive manufacturing techniques, such as 3D printing with spatially varying infill densities and multi-material inkjet deposition, allow precise realization of complex dielectric profiles [6], [7], [8]. Complementing these approaches, metamaterial-inspired designs employing subwavelength unit cells offer an effective means to achieve smoothly graded refractive indices [9], [10]. For terahertz applications, layered manufacturing methods combining laser-cut dielectric sheets into stacked assemblies have proven effective, though they introduce some anisotropy. Advances in ceramic stereolithography now offer promising avenues for fabricating high-permittivity GRIN structures at millimeter-wave frequencies, helping bridge the gap between theoretical designs and practical, manufacturable components.

Synthesis methods for GRIN lenses can be broadly classified into two categories. The first category allows the direct analytical determination of the refractive index profile, whereas the second category relies on optimization techniques that iteratively employ analysis methods based on GO.

The first category encompasses the Abel inversion method (AIM) and transformation optics (TO). AIM applies Fermat's principle to curvilinear ray paths, yielding closed-form solutions for canonical lenses such as the Luneburg and Maxwell fish-eye designs [11], [12]. However, AIM is restricted to symmetric geometries that preserve ray momentum. TO exploits coordinate transformations to achieve novel functionalities, including flattened Luneburg lenses [13], but typically requires anisotropic materials that complicate fabrication and can compromise bandwidth.

Within the second category, numerical optimization plays a central role. Population-based algorithms, such as particle swarm optimization (PSO) [14] and genetic algorithms (GA) [15], enable systematic exploration of the GRIN lens design space, accommodating multi-objective constraints and fabrication-aware discretization. Gradient-based methods, particularly adjoint optimization, have proven highly effective in shaping index distributions to achieve far-field performance targets [16], [17]. Nevertheless, as iterative approaches, they are computationally intensive and susceptible to convergence toward local minima.

The method presented in this paper, namely the phase tracing method (PTM), belongs to the second category of synthesis techniques, which provide direct analytical determi-

---

This work was supported by Huawei inside the framework of the Huawei - University of Siena Joint Lab.

The authors are with the Department of Information Engineering and Mathematics, University of Siena, Siena, 53100, Italy (e-mail: ilir.gashi2@unisi.it).

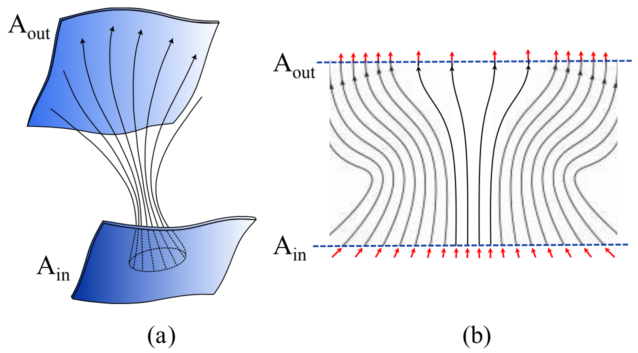

Fig. 1: Illustration of the refractive index retrieval problem: (a) The input ray directions are defined on curved surfaces A_{in} and A_{out}. The rays between these surfaces form a bundle whose density and curvature dictate the refractive index variations. (b) Cross-section of an azimuthally symmetric ray bundle with flat input and output surfaces, yielding a refractive index distribution independent of the azimuthal angle ϕ.

nation of the graded-index profile. PTM introduces a synthesis framework that overcomes the limitations of existing design approaches by reformulating the problem through an inverse strategy. By reversing the conventional GO analysis paradigm, the method computes the refractive index distribution directly from predefined ray trajectories, enabling deterministic transformation of input fields into desired aperture profiles. Unlike TO-based approaches, PTM does not require anisotropic materials, while retaining the analytical transparency of a closed-form design. Moreover, it is applicable to any index variation that supports a ray-type description, without being restricted to the momentum-conserving variations required by AIM.

The paper is organized as follows. Section II outlines the theoretical foundations of the direct synthesis methodology, presenting phase control (Section II-A), amplitude control (Section II-B), and clothoid ray trajectories (Section II-C). Section II-D details the overall GRIN lens synthesis algorithm and Section II-E presents a detailed technical comparison with existing inverse methods. Section III presents comprehensive numerical validations: Section III-A retrieves the Maxwell Fish Eye lens profile to verify the analytical approach; Section III-B demonstrates a telescopic GRIN lens design; Section III-D illustrates near-field focusing through Hankel distribution synthesis for Bessel beam generation; and Section III-E showcases a rectangular-to-uniform circular 3D lens transformation. Collectively, these developments advance GRIN lens design by providing a versatile framework that combines analytical precision with practical implementation for next-generation electromagnetic systems.

II. FORMULATION

This section outlines the theoretical foundation of the PTM. The objective is to design an inhomogeneous, isotropic, and lossless dielectric lens that transforms a specified incident ray field at the input surface, A_{in}, into a prescribed output ray field at A_{out}, controlling the ray trajectories within the enclosed volume V. As depicted in Fig. 1(a), the lens volume is bounded by the surfaces A_{in} and A_{out}, and may optionally include an orthogonal lateral surface A_{ℓ}. The medium is characterized by a spatially varying refractive index $n(\mathbf{r}) = \sqrt{\varepsilon_r(\mathbf{r})}$.

The boundary conditions for this problem are defined by the ray direction and the ray density (or power distribution) at both the input and output interfaces. While many practical GRIN lens applications feature flat interfaces, this specific geometry is not a fundamental restriction of the PTM framework.

Although the core formulation can be presented for general three-dimensional geometries, we initially focus on the computationally tractable case of azimuthally symmetric index profiles. This approach reduces the synthesis problem to a two-dimensional analysis in the plane of revolution, where ray trajectories can be visualized as shown in Fig. 1(b). The PTM framework remains fully extensible to arbitrary 3D configurations, as demonstrated in Section III-E through the design of a lens that transforms a rectangular waveguide mode to a uniform circular aperture. In such 3D scenarios, the synthesis is performed on multiple angular cuts in the ϕ-plane, with the refractive index profile determined by enforcing power conservation and phase matching across all sections.

A. Phase Control

The core objective is to transform an input wavefront ψ_{in} at the entrance aperture A_{in} into a desired output wavefront ψ_{out} at the exit aperture A_{out} through controlled propagation within the lens volume. This wavefront transformation is physically realized by strategically shaping ray trajectories, which are orthogonal to the wavefronts. For an azimuthally symmetric lens, we consider a two-dimensional cross-section in the ρ-z plane, where z is the axial coordinate and ρ is the radial coordinate. In this plane, we parameterize a family of ray trajectories as

$$\mathbf{r}(t,p) = \rho(t,p)\hat{\boldsymbol{\rho}} + z(t,p)\hat{\mathbf{z}}, \tag{1}$$

where the parameter t varies along each individual ray, and p labels different rays in the family. When ray trajectories are simple and smooth, (1) establishes a diffeomorphism between the parametric space (t,p) and the geometrical space (ρ,z). While ray trajectories are the mapping of the $p = const$ lines, wavefronts have not a simple counterpart in the parameter space. In fact, constant t curves are not in general wavefronts and are not orthogonal to the rays. For each ray, we define the arc length s measured along the ray, with the unit tangent vector given by

$$\hat{\mathbf{s}} = \frac{d\mathbf{r}}{ds} = \frac{\partial\mathbf{r}/\partial t}{|\partial\mathbf{r}/\partial t|}. \tag{2}$$

As discussed in [1] [Sec. 3.2.3], a physically realizable family of rays in an inhomogeneous isotropic medium must form a normal ray congruence, meaning that the tangent field satisfies $\hat{\mathbf{s}} \cdot (\nabla \times \hat{\mathbf{s}}) = 0$, which guarantees the existence of wavefronts orthogonal to the rays.

In geometrical optics (GO), the field is split into the product of a slowly varying vector amplitude and a rapidly varying phase

$$\mathbf{E}(\mathbf{r}) = \mathbf{E}_0(\mathbf{r})e^{-jk\psi(\mathbf{r})} \tag{3}$$

This article has been accepted for publication in IEEE Transactions on Antennas and Propagation. This is the author's version which has not been fully edited and content may change prior to final publication. Citation information: DOI 10.1109/TAP.2026.3676548

in which wavefronts are described by isosurfaces of the eikonal phase function $\psi(\mathbf{r})$, obeying to the Eikonal equation

$$|\nabla\psi(\mathbf{r})| = n(\mathbf{r}), \tag{4}$$

with $n(\mathbf{r})$ denoting the refraction index at any point in the inhomogeneous medium. In GO, the Eikonal equation (4) is solved by using the method of the charactristics; i.e., by defining rays such that $\nabla\psi = n\hat{\mathbf{s}}$, which can be traced by solving the ray equation

$$\frac{d}{ds}\left(n\hat{\mathbf{s}}\right) = \nabla n \tag{5}$$

for a given starting point and initial direction. The ray equation (5) is simply derived by taking the gradient of the square of the Eikonal equation (4). Expanding (5) and using the fact that $dn/ds = \nabla n \cdot \hat{\mathbf{s}}$, we obtain

$$\frac{d\hat{\mathbf{s}}}{ds} = (\underline{\mathbf{1}} - \hat{\mathbf{s}}\hat{\mathbf{s}}) \cdot \nabla \ln n. \tag{6}$$

Next, by recalling that the curvature vector of a ray is defined as $\mathbf{K} = d\hat{\mathbf{s}}/ds = \kappa\hat{\boldsymbol{\nu}}$, where κ is the scalar curvature and $\hat{\boldsymbol{\nu}}$ is the unit normal vector to the ray pointing toward the center of curvature, the curvature - refractive index relationship is obtained

$$\kappa = \nabla(\ln n) \cdot \hat{\boldsymbol{\nu}}. \tag{7}$$

Therefore, the refractive index can be retrieved by integrating (7) along a wavefront. Since wavefronts are not directly available from (1), the following procedure was established to trace wavefronts. Let ℓ denote the arc length along a wavefront, and let u be a parameter that labels different wavefronts. A point on a wavefront can be expressed as $\mathbf{q}(\ell, u)$. Since the tangent to the wavefront, $d\mathbf{q}/d\ell$, must be perpendicular to $\hat{\mathbf{s}}$, we have the ordinary differential equation (ODE)

$$\frac{d\mathbf{q}}{d\ell} = \hat{\mathbf{s}} \times \hat{\boldsymbol{\phi}}, \tag{8}$$

where $\hat{\boldsymbol{\phi}}$ is the azimuthal unit vector (out-of-plane direction in the 2D cross-section). For planar ray congruences, the binormal vector $\hat{\mathbf{b}}$ is constant and equal to $-\hat{\boldsymbol{\phi}}$. Integrating (7) along a wavefront from a reference point $\mathbf{q}_0$ to a point $\mathbf{q}$ yields the refractive index distribution on that wavefront

$$\int_{\mathbf{q}_0}^{\mathbf{q}} \nabla(\ln n) \cdot d\mathbf{q} = \int_{\ell_0}^{\ell} \kappa(\ell')\, d\ell', \tag{9}$$

$$n(\ell, u) = n_0(u) \exp\left(\int_{\ell_0}^{\ell} \kappa(\ell', u)\, d\ell'\right), \tag{10}$$

where $n_0(u) = n(\ell_0, u)$ is an arbitrary value of the refractive index at the starting point $\mathbf{q}_0$, which can be selected to keep the refractive index in a feasibility range (e.g., $\min_{\ell}\{n(\ell, u)\} \geq 1$). Equation (10) is the cornerstone of the PTM: it provides a direct analytical relationship between the ray curvature field κ and the refractive index profile n. Once the ray trajectories (and hence their curvatures) are specified, the index distribution can be computed by integrating along wavefronts. The fact that only the transverse component to the ray of the gradient of the refractive index is constrained by (7), while the component along the ray dn/ds is unconstrained, physically corresponds to the fact that enforcing the ray trajectories does not dictate the velocity with which those trajectories are followed. Different velocities along the same ray paths would result in different refractive index profiles. This degree of freedom corresponds the arbitrary n_0 factor in (10). The exponential relationship in (10) enables precise phase control by linking ray curvature to refractive index gradients. By selecting ray trajectories with low curvature, one can minimize index variations, facilitating fabrication. In Section II-C, we introduce clothoid curves as a particularly advantageous family of ray trajectories that yield smooth, bounded index gradients.

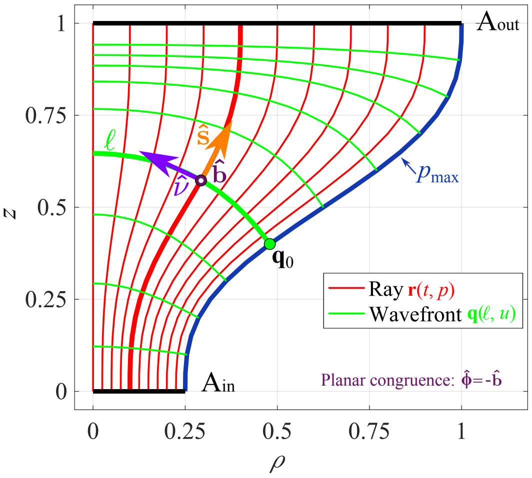

Fig. 2: Geometry of the problem: ray trajectories (red solid lines) and wavefronts (green solid lines) in a 2D cross-section. The ray family is parameterized by label p, with $p_{\max}$ denoting the outermost ray. At the intersection of a ray and wavefront, $\hat{\mathbf{s}}$ is the unit tangent to the ray, $\hat{\nu}$ is the unit normal to the ray (tangent to the wavefront), and $\hat{\mathbf{b}} = -\hat{\boldsymbol{\phi}}$ is the out-of-plane binormal (azimuthal unit vector). The wavefront arc length ℓ and the starting point $\mathbf{q}_0$ are also indicated.

The geometry of rays and wavefronts, including the relevant vectors and parameters, is illustrated in Fig. 2. As noted, for planar ray congruences the binormal vector $\hat{\mathbf{b}}$ coincides with the azimuthal unit vector $-\hat{\boldsymbol{\phi}}$ (pointing out of the page), and the outermost ray is labeled $p_{\max}$. The ray family extends from $p = 0$ to $p = p_{\max}$, where $p_{\max}$ corresponds to the lateral boundary of the lens.

B. Amplitude Control

The precise transformation of electromagnetic field amplitudes through a GRIN lens is fundamentally governed by the principle of power conservation in ray tubes, a core tenet of GO for lossless media. When an inhomogeneous lens transforms an input field distribution to a target output profile, it must redistribute the power without dissipation, maintaining total power flow while adapting to spatial scaling requirements. This energy redistribution manifests as controlled expansion or compression of ray tubes, infinitesimal bundles of rays propagating through the lens volume, where changes in ray density directly correspond to amplitude variations.

The field amplitude transformation is therefore expressed as

$$I_{\text{in}}(x_{\text{in}})dx_{\text{in}} = I_{\text{out}}(x_{\text{out}})dx_{\text{out}}, \tag{11}$$

where $I_{\text{in}}(x) \propto |f_{\text{in}}(x)|^2$ and $I_{\text{out}}(x) \propto |f_{\text{target}}(x)|^2$ are the power densities at the input (A_{in}) and output (A_{out}) planes, respectively. The ray mapping function $x_{\text{out}} = \mathcal{M}(x_{\text{in}})$, which defines how points on the output plane connect to points on the input plane via ray trajectories within the lens, is determined through cumulative power distributions

$$C_{\text{in}}(x_{\text{in}}) = \int_0^{x_{\text{in}}} I_{\text{in}}(u)du, \quad C_{\text{out}}(x_{\text{out}}) = \int_0^{x_{\text{out}}} I_{\text{out}}(v)dv, \tag{12}$$

satisfying $C_{\text{in}}(x_{\text{in}}) = C_{\text{out}}(x_{\text{out}})$, which implicitly defines the mapping $x_{out} \leftrightarrow x_{in}$

$$x_{\text{out}} = \mathcal{M}(x_{\text{in}}) = C_{\text{out}}^{-1}\left(C_{\text{in}}(x_{\text{in}})\right). \tag{13}$$

The field amplitude transformation is then given by

$$|f_{\text{out}}(x_{\text{out}})|^2 = |f_{\text{in}}(x_{\text{in}})|^2 \left|\frac{dx_{\text{in}}}{dx_{\text{out}}}\right|, \tag{14}$$

where the Jacobian determinant $|J| = |dx_{\text{in}}/dx_{\text{out}}|$ quantifies ray tube expansion (when $|J| < 1$) or contraction (when $|J| > 1$). The amplitude control complements the phase manipulation, allowing simultaneous synthesis of both magnitude and phase in the output aperture field by resorting to the PTM.

C. A Convenient Choice: Clothoid Trajectories

In the context of PTM-based lens synthesis, the selection of ray trajectories is fundamental, as these define the phase evolution and refractive index gradient via the curvature field (10). A particularly advantageous class of curves for this purpose is the clothoid (Euler or Cornu spiral) [18], which is defined by the property that its curvature κ varies linearly with arc length ℓ. This property ensures a smooth and gradual bending of rays, resulting in minimal and continuous variations in the refractive index, an essential feature for practical GRIN lens implementation.

To mathematically describe a clothoid in two-dimensional space, we adopt a complex representation of the position vector

$$\mathbf{r}(t) = x(t)\hat{\mathbf{x}} + y(t)\hat{\mathbf{y}} \quad \longrightarrow \quad z(t) = x(t) + jy(t), \tag{15}$$

where t is the curvilinear abscissa, or arc length, and $z(t) \in \mathbb{C}$ is the complex representation of the spatial trajectory.

The clothoid is defined via its integral form

$$z(t) = z_0 + \int_0^t e^{j\theta(\tau)}d\tau, \tag{16}$$

where z_0 is the initial point of the trajectory, and $\theta(t)$ is the local angle of the tangent vector to the curve at position t. The first derivative gives the unit tangent vector

$$\frac{dz(t)}{dt} = e^{j\theta(t)}. \tag{17}$$

The second derivative gives the curvature vector

$$\frac{d^2z(t)}{dt^2} = \theta'(t)e^{j\left[\theta(t)+\frac{\pi}{2}\right]}, \tag{18}$$

and the amplitude of this expression corresponds to the local curvature

$$\kappa(t) = \frac{d\theta(t)}{dt}. \tag{19}$$

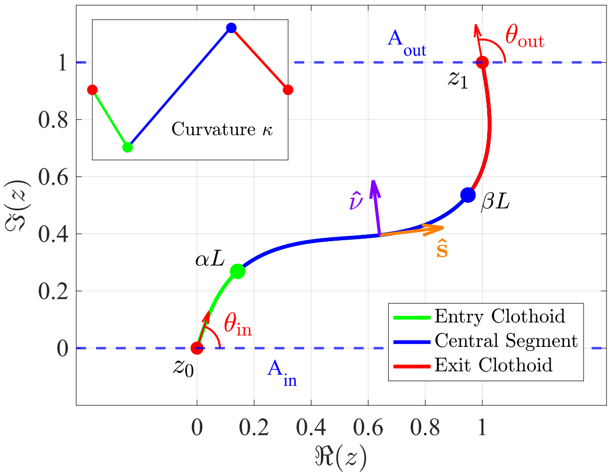

Fig. 3: Piecewise clothoid trajectory in the complex plane $\mathbb{C}$: the path begins at a point $z_0 \in A_{in}$, with an initial direction θ_0. The first clothoid segment (green solid line) ends at the junction point αL, where L denotes the total length of the clothoid. The second segment (blue solid line) continues to the next junction point βL, leading into the final clothoid segment (red solid line), which terminates at the point $z_1 \in A_{\text{out}}$, with a final direction θ_{out}. The inset in the top-left corner illustrates the curvature k along the trajectory, highlighting its linear progression.

This linearity of curvature naturally complements the PTM formulation, in which the logarithmic gradient of the refractive index is directly proportional to the ray curvature, as shown in (7). Therefore, clothoid rays inherently promote refractive index profiles with bounded gradients and smooth variations.

A powerful tool for constructing such clothoid curves under practical boundary constraints is the G2 Hermite problem [19]. This problem involves synthesizing an interpolating curve between two endpoints z_0 and z_1 with specified tangent angles θ_{in}, θ_{out} and curvatures κ_{in}, κ_{out} at both ends. The general solution involves a piecewise composition of three clothoid segments, as illustrated in Fig. 3, where the parameters α and β define the junction points of these segments. The total arc length L is determined to ensure

$$\int_0^L \kappa(\tau)d\tau = \theta_1 - \theta_0, \tag{20}$$

as well as $z(L) = z_1$. Solving this system yields the continuous curvature profile $\kappa(t)$ along the entire ray trajectory, suitable for direct use in the PTM framework.

The inherent smoothness and compatibility of clothoids with the PTM equations enable analytical, fabrication-friendly synthesis of lenses with reduced refractive index distributions, making them a convenient choice for practical GRIN lens implementations.

D. GRIN Lens Overall Design Algorithm

The PTM GRIN Lens Design algorithm begins by performing a *power mapping* between the input and target field distributions, and the normalized power profiles I_{in} and I_{out} are computed. The cumulative distributions of C_{in} and C_{out}, are then calculated and used to establish a mapping from the

This article has been accepted for publication in IEEE Transactions on Antennas and Propagation. This is the author's version which has not been fully edited and content may change prior to final publication. Citation information: DOI 10.1109/TAP.2026.3676548

Algorithm 1 Phase-Tracing GRIN Lens Design

```
Require:
    $a, b, d$: Input width, output width, lens thickness
    $E_{\text{target}}(x)$: Desired field at target plane
    $N_p$: Number of rays
    $N_t$: Number of sample points per ray
    // power mapping
$I_{\text{in}} \leftarrow |f_{\text{in}}|^2 / \int |f_{\text{in}}|^2 dx$
$I_{\text{out}} \leftarrow |f_{\text{target}}|^2 / \int |f_{\text{target}}|^2 dx$
$C_{\text{in}}(x) \leftarrow \int_0^x I_{\text{in}}(\xi) d\xi$
$C_{\text{out}}(x) \leftarrow \int_0^x I_{\text{out}}(\xi) d\xi$
$x_{\text{out}} \leftarrow C_{\text{out}}^{-1}\left(C_{\text{in}}(x_{\text{in}})\right)$
    // phase mapping
$\Psi_{\text{in}} \leftarrow$ Input eikonal distribution
$\Psi_{\text{out}} \leftarrow$ Output eikonal distribution
    // ray tracing
for $i \leftarrow 1$ to $N_p$ do
    $(\mathbf{r}_i, \kappa_i) \leftarrow \text{Clothoids}(x_{\text{in},i}, y_{\text{in},i}, x_{\text{out},i}, y_{\text{out},i}, \Psi_{\text{in},i}, \Psi_{\text{out},i})$
end for
    // phase tracing
for $j \leftarrow 1$ to $N_t$ do
    $\mathbf{q}_0 \leftarrow \mathbf{r}_{N_p}(j)$ {Start from output}
    $\mathbf{g}_j \leftarrow \text{ODE}(d\mathbf{q}/ds, \mathbf{q}_0)$
    for $i \leftarrow 1$ to $N_p$ do
        $\mathbf{p}_{ij} \leftarrow \mathbf{r}_i \cap \mathbf{g}_j$ {Ray-wavefront intersection}
        $[\mathbf{x}_{\text{up}}(i,j), \mathbf{y}_{\text{up}}(i,j)] \leftarrow \mathbf{p}_{ij}$
    end for
    $\mathbf{c}_j \leftarrow \text{interpCurvature}(\mathbf{p}_{ij}, \kappa_i)$
    $\mathbf{n}_{\text{up}}(:,j) \leftarrow \exp(\int \mathbf{c}_j ds)$
    $\mathbf{n}_{\text{up}}(:,j) \leftarrow \mathbf{n}_{\text{up}}(:,j) / \min\left[\mathbf{n}_{\text{up}}(:,j)\right]$
end for
    // refractive index interpolation
$\mathbf{n}(x,y) \leftarrow \text{interp}(\mathbf{x}_{\text{up}}, \mathbf{y}_{\text{up}}, \mathbf{n}_{\text{up}}, \mathbf{x}, \mathbf{y})$
$\varepsilon_r(x,y) \leftarrow \mathbf{n}^2(x,y)$
```

input points x_{in} to the output points x_{out} that preserves the power flow.

Next, the algorithm sets the input and output eikonal (phase gradient) distributions, Ψ_{in} and Ψ_{out}, which define the direction of the rays on the input A_{in} and output A_{out} surfaces. Using these, for each ray i (out of N_p total rays), a clothoid curve is generated by connecting the input and output points with specified initial and final directions. The function `clothoids` from [20] is used to generate the curve $\mathbf{r}_i$ and the corresponding curvature κ_i, which defines the bending required for each ray trajectory.

The *phase tracing* step involves propagating wavefronts from the output ray by numerically solving the ODE (8) for the wavefront curves $\mathbf{g}_j$, sampled at N_t points. At each wavefront point, intersections $\mathbf{p}_{ij}$ with all rays $\mathbf{r}_i$ are determined to establish the spatial sampling grid. The local curvature values are interpolated at these intersection points to calculate the refractive index profile along each wavefront via (10). The refractive index profiles are normalized relative to the minimum desired values n_0 to ensure physical consistency.

Finally, the discrete refractive index samples $\mathbf{n}_{\text{up}}$ on the wavefront grid are interpolated over the entire lens domain to produce a continuous refractive index distribution $\mathbf{n}(x,y)$, from which the relative permittivity $\varepsilon_{\text{r}}(x,y) = \mathbf{n}^2(x,y)$ is derived. This procedure yields a graded-index lens design that transforms the input field into the desired output distribution following the PTM framework. The detailed algorithmic procedure is presented in Algorithm 1.

E. Comparison with Existing Inverse Methods

The PTM distinguishes itself from established inverse design approaches in several key aspects. Transformation optics (TO) [21], [22] and numerical optimization [14], [17] represent the dominant paradigms, while Abel-type inversions [11], [23] and analytical ray-prescription methods [24], [25] provide specialized solutions.

TO derives material parameters from coordinate mappings, enabling advanced functionalities such as flattened Luneburg lenses [13]. Nevertheless, this framework generally results in anisotropic and magneto-dielectric material prescriptions, which substantially complicate fabrication and limits operational bandwidth. In many practical implementations, substantial simplifications are introduced by neglecting anisotropy and magnetic response, which breaks the strict correspondence with the original transformation and introduces errors on the electromagnetic response that are difficult to predict.

In contrast, PTM is explicitly grounded in GO, as it directly synthesizes the refractive index profile from prescribed ray trajectories and phase evolution. By operating within the GO regime and employing purely isotropic graded-index distributions, PTM avoids artificial magnetism and tensor anisotropy, preserves the intrinsic broadband nature of GRIN media, and provides a more controlled and fabrication-oriented approach to wavefront engineering.

Numerical optimization, whether population-based [14], [15] or gradient-based [16], [17], iteratively adjusts index distributions to meet electromagnetic targets. While flexible for complex constraints, these methods are computationally intensive and prone to local minima. PTM provides deterministic, non-iterative synthesis with analytical transparency, eliminating computational bottlenecks while offering physical insight into ray-material relationships.

The Abel Inversion Method (AIM) [11] solves the inverse problem for rotationally symmetric media, producing canonical solutions like Luneburg and Maxwell fish-eye lenses. Recent extensions focus on index reconstruction from measured ray deviations [26], [27] but remain confined to symmetric geometries. PTM removes this symmetry restriction entirely, enabling synthesis of arbitrary asymmetric profiles while maintaining analytical tractability through the curvature-index relationship.

Analytical ray-prescription methods provide the closest precedent to PTM. In [25], the authors derived index distributions for given one-parameter ray families, while in [24] it is presented how to obtain profiles producing prescribed two-dimensional paths using conformal mapping. In [28], the authors provided mathematical comparison between Fermat's

This article has been accepted for publication in IEEE Transactions on Antennas and Propagation. This is the author's version which has not been fully edited and content may change prior to final publication. Citation information: DOI 10.1109/TAP.2026.3676548

principle and eikonal equation formulations. However, these methods share critical limitations: they typically operate within paraxial approximations, prescribe limited ray families without full wavefront control, and lack amplitude transformation capabilities. PTM transcends these limitations by (1) operating beyond paraxial regimes through exact GO relations, (2) providing complete wavefront synthesis via clothoid ray bundles, (3) enforcing power conservation for amplitude control, and (4) explicitly linking curvature to index gradients through exponential integration that guarantees smooth, fabricable profiles.

In summary, PTM occupies a unique position by combining the analytical rigor of Abel-type methods with the flexibility of TO, while avoiding the computational burden of optimization and the limitations of earlier ray-prescription approaches. This enables deterministic synthesis of isotropic, manufacturable GRIN lenses for complex wavefront transformations across microwave and optical domains.

III. NUMERICAL EXAMPLES

This section demonstrates the capabilities of the PTM through practical GRIN lens implementations. We first validate the analytical framework by recovering the refractive index profile of the Maxwell Fish Eye lens. Subsequently, we present four advanced GRIN lens designs: a telescopic GRIN lens achieving 2× aperture magnification, a flat-top beam generator with uniform ±15° coverage, a Bessel beam launcher for non-diffracting radiation, and a GRIN lens transforming a rectangular waveguide mode into a uniform circular aperture. Each design addresses distinct electromagnetic manipulation challenges while showcasing the PTM's versatility across different application domains.

A. Closed Form GRIN test: Maxwell Fish Eye Lens

As a validation of the PTM, we derive here the refractive index distribution of the well-known Maxwell fish eye (MFE) lens [12], a classical GRIN structure capable of achieving perfect imaging in the geometrical optics limit. The MFE is defined as a spherical region of radius a, centered at the origin in the ρ-z plane. We consider a point source located at $\mathbf{r}_0 = -a\hat{\mathbf{z}}$, launching rays that follow circular trajectories. Each ray path lies on a circle centered at $C = -a\cot\theta_0\hat{\boldsymbol{\rho}}$, where θ_0 is the initial launch angle of the ray. The radius of the path of the rays is given by $R = a\ \csc\theta_0$. The corresponding wavefronts are also circular and centered at a point C along the z-axis, with radius $R = \sqrt{c^2 - a^2}$, as illustrated in Fig. 4. According to the PTM formulation, the curvature κ of the rays determines the gradient of the refractive index (7), and the refractive index is retrieved by integrating the curvature along the wavefront (equation (10)). The initial angle of the ray at radial position ρ is given by $\theta_0 = \arctan\left(\frac{2a\rho}{a^2-\rho^2-z^2}\right)$ which in the equatorial plane $z = 0$, simplifies to $\sin\theta_0 = \frac{2a\rho}{a^2+\rho^2}$, yielding to the ray curvature

$$\kappa(\rho, z = 0) = \frac{\sin\theta_0}{a} = \frac{2\rho}{a^2+\rho^2}, \tag{21}$$

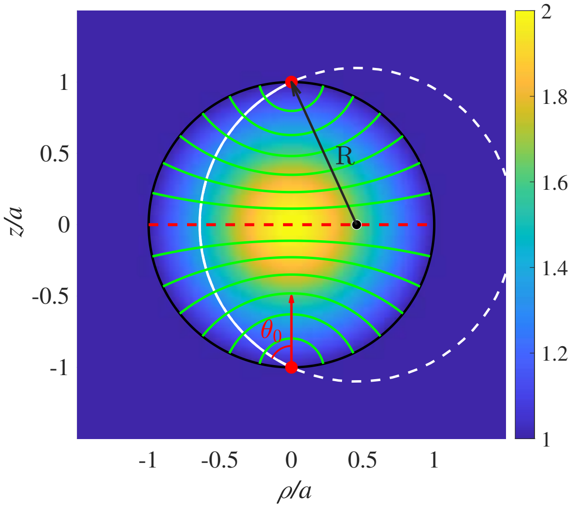

Fig. 4: Phase tracing in a Maxwell Fish Eye (MFE) lens in a vertical plane, with the source located at the "south pole" $\mathbf{r}_0 = -a\hat{\mathbf{z}}$. The background color represents the refractive index n, with the surrounding medium having $n = 1$ outside the MFE boundary (black line). The analytically retrieved wavefronts are shown as green solid lines, along with a highlighted ray (white solid line) whose trajectory follows an arc of a circle with radius R, centered at $C = -a\cot\theta_0\hat{\boldsymbol{\rho}}$, where θ_0 denotes the initial direction of the ray within the MFE. The red dashed line indicates the location at which the PTM is applied to reconstruct the refractive index distribution of the MFE.

which is used in the PTM to compute the refractive index distribution.

By integrating this curvature along the wavefront as shown in (10), and assuming the central refractive index value $n(0) = 2$, the refractive index is given by

$$n(\rho) = 2\exp\left(-\int_0^{\rho} \frac{2\rho'}{a^2+\rho'^2}\,d\rho'\right) = \frac{2}{1+\left(\frac{\rho}{a}\right)^2}, \tag{22}$$

which is the analytical solution for the MFE lens refractive index profile. This example demonstrates that the PTM can recover the analytical refractive-index profile of the Maxwell fish-eye lens directly from its known ray curvatures. More generally, whenever the ray curvature can be expressed in analytical form, the PTM provides a straightforward route to deriving closed-form GRIN profiles. In this sense, the PTM offers a practical and versatile alternative to the classical Abel-transform–based inversion methods for GRIN.

B. Telescopic Lenses

As a first design example, we present the refractive-index synthesis of a telescopic lens [29]. Telescopic lenses have been known for more than four centuries, originating from Galileo's pioneering work on refracting telescopes [30]. In their conventional implementation, telescopic systems are formed by cascading a diverging and a converging lens. Developing an equivalent continous GRIN implementation, however, remains a significant challenge despite the potential advantages in compactness, efficiency, and wavefront quality. A non-conventional GRIN telescopic configuration, based on a cascade of diverging and converging cylindrical GRIN elements, was proposed in [31], where closed-form analytical expressions were derived. Nevertheless, the solution

This article has been accepted for publication in IEEE Transactions on Antennas and Propagation. This is the author's version which has not been fully edited and content may change prior to final publication. Citation information: DOI 10.1109/TAP.2026.3676548

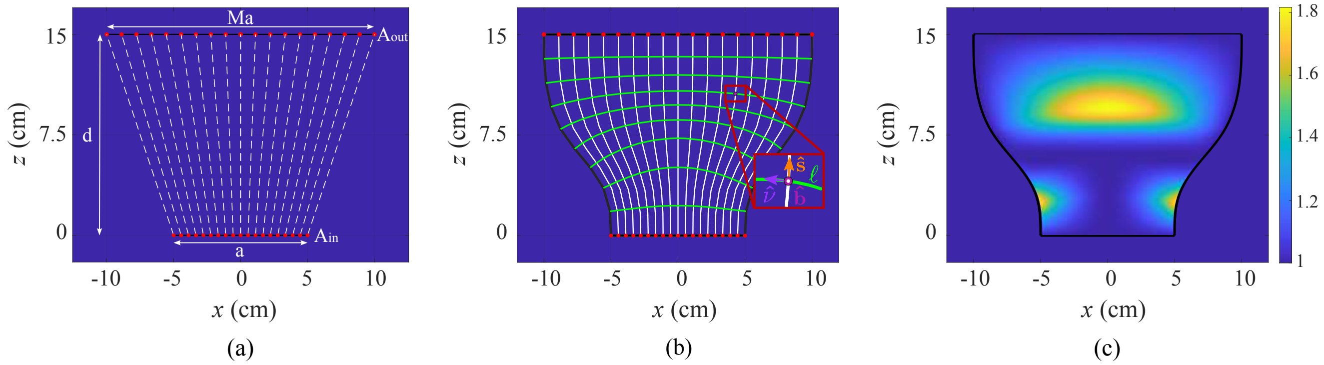

(a) (b) (c)

Fig. 5: Refractive index retrieval of the telescopic lens: (a) ray mapping (both amplitude and phase) is performed to determine the output points in $\mathrm{A_{out}}$, thereby realising the desired transformation from $\mathrm{A_{in}}$; (b) the corresponding rays are connected using clothoid trajectories (white solid lines), and the associated wavefronts are reconstructed (green solid lines) by integrating (8) from the lateral boundary inward; (c) the PTM is then applied to compute the refractive index distribution, shown in the background of the plot. Lens boundaries are outlined in black.

in [31] introduces an interface between the two GRIN sections, which may cause reflections and mode mismatch. A fully continuous GRIN lens capable of achieving telescopic aperture magnification without internal interfaces is therefore highly desirable. and the solution developed here provides an elegant and practical approach to this longstanding problem.

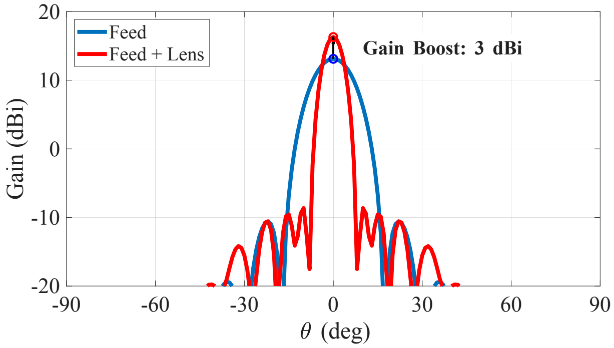

Fig. 6: CST simulation results showing the gain (in dBi) in the $\phi = 0$ plane for: (a) the TE_{10} feed alone (blue solid line), and (b) the feed combined with the telescopic lens (red solid line). The observed gain enhancement is approximately 3 dBi, which matches the theoretical expectation of 3 dBi for a telescopic lens with magnification $M = 2$.

A telescopic lens provides an aperture magnification by transforming an input aperture of width a into an expanded output aperture of width Ma, where $M > 1$ is the magnification factor. This expansion leads to significant performance enhancement: the effective aperture area increases by M^2, corresponding to a theoretical maximum gain improvement of $10\log_{10} M$ dB. Furthermore, the beamwidth is reduced by a factor of M. The telescopic lens synthesized here has an input aperture $\mathrm{A}_{in} = a = 10$ cm and an output aperture of $\mathrm{A}_{out} = Ma = 20$ cm (with $M = 2$).

The synthesis follows the Algorithm 1 through the following structured steps, each directly linked to the corresponding equations and to Fig. 5:

1) *Ray mapping (Algorithm 1, lines 1–5).* The input power density is given by the TE_{10} mode profile $I_{\text{in}}(x_{\text{in}}) \propto \cos^2(\pi x_{\text{in}}/a)$. The target output is a uniform plane wave, hence $I_{\text{out}}(x_{\text{out}})$ is constant over $|x_{\text{out}}| \leq Ma/2$. Equating the cumulative power distributions C_{in} and C_{out} (Sec. II-B) yields the linear mapping $x_{\text{out}} = Mx_{\text{in}}$. The amplitude then scales as $|f_{\text{out}}| = |f_{\text{in}}|/\sqrt{M}$ via (14), exactly conserving energy. The ray endpoints are shown in Fig. 5(a).
2) *Clothoid ray construction (Algorithm 1, lines 8–12).* For each ray indexed by its input coordinate $x_{\text{in}}^{(i)}$, the start point $(x_{\text{in}}^{(i)}, 0)$, end point $(Mx_{\text{in}}^{(i)}, d)$, boundary angles $\pi/2$, and zero curvatures are supplied to the G^2 Hermite clothoid solver (Sec. II-C). The junction parameters α, β are chosen to minimise the maximum absolute curvature, yielding a smooth curvature profile $\kappa_i(s)$ that varies linearly with arc length s (Eq. (19)). The resulting ray family appears in Fig. 5(b).
3) *Wavefront construction (Algorithm 1, lines 13–15).* Wavefronts are generated by integrating the wavefront-tracing ODE (8) inward from the lateral boundary traced by the outermost ray ($i = N_p$). With the initial condition $\mathbf{q}_0 = \mathbf{r}_{N_p}(s)$, integration produces a family of wavefronts $\mathbf{q}(\ell)$ parameterised by arc length ℓ. These wavefronts, orthogonal to the ray bundle by construction, are drawn as green solid lines in Fig. 5(b).
4) *Refractive index integration (Algorithm 1, lines 16–22).* For each wavefront, intersections with all rays are computed, forming a curvilinear grid. Curvature values $\kappa_i(s)$ are interpolated onto the grid points, and the exponential integral (10) is evaluated along the wavefront. The reference index $n(\ell_0)$ at the intersection with the outermost ray is scaled so that $\min n = 1$ throughout the lens.
5) *Continuous profile reconstruction (Algorithm 1, lines 24–25).* The discrete refractive index samples (x, y, n) on the curvilinear grid are interpolated onto a regular Cartesian mesh covering the entire lens volume. This produces a smooth, continuous distribution $n(x, y)$, shown in Fig. 5(c).

This deterministic, non-iterative procedure demonstrates the directness of the PTM: each design quantity follows explicitly from the prescribed ray data.

Simulation validation: A parallel-plate waveguide was mod-

This article has been accepted for publication in IEEE Transactions on Antennas and Propagation. This is the author's version which has not been fully edited and content may change prior to final publication. Citation information: DOI 10.1109/TAP.2026.3676548

eled in CST Microwave Studio at 15 GHz and filled with the synthesized GRIN profile. Excited by the TE_{10} mode, the structure yields the gain patterns at $\phi = 0$ of the feed with and without the lens are shown in Fig. 6. The observed gain enhancement of 3.1 dBi agrees with the theoretical $10\log_{10}2 = 3.01$ dBi, confirming the intended 2× aperture magnification.

C. Flat-Top Beam Lenses

The PTM, being a general design methodology, allows the realization of arbitrary field transformations. In this example, we address a more challenging case: the synthesis of a flat-top beam, using the same parallel-plate waveguide (PPW) configuration as in the previous section, excited by the fundamental TE_{10} rectangular mode.

Flat-top beam synthesis addresses a critical need in radar and communication systems by generating far-field radiation patterns with uniform intensity over a specified angular sector. Broad beams or flat-top radiation patterns are engineered to provide uniform coverage within a specified angular sector while ensuring a rapid roll-off of radiated power outside this region. Various approaches can be used to shape the beam, including lenses [32], [33], antenna arrays with prescribed amplitude and phase excitations [34], [35], or leaky-wave antenna arrays [36]. Here, we introduce a novel GRIN lens approach that transforms the fundamental TE_{10} mode profile into an optimized aperture distribution, which inherently produces a flat-top pattern spanning $\theta \in [-15°, 15°]$. The output field distribution is derived via spectral propagation of the ideal sinc-based pattern, explicitly accounting for the output aperture width b.

At $z = 0$, the reference aperture field $E_{\mathrm{ref}}(x) \propto \operatorname{sinc}\left(\frac{\pi x}{\beta}\right)$ contains sign reversals (negative amplitudes) in its sidelobes. Direct implementation would require π-phase shifts (equivalent to $\lambda_0/2$ path delays) at the sign-change boundaries, introducing frequency-dependent path differences that fundamentally limit lens bandwidth. By propagating to $z_0 > 0$, the field is transformed into a complex distribution where the amplitude $|E_{\mathrm{out}}(x)|$ becomes a broad tapered distribution with no nulls but only with a limited ripple, and the phase $\phi_{\mathrm{quad}}(x) = \arg\{E_{\mathrm{out}}\}$ evolves smoothly eliminating sign-reversal. This approach eliminates phase discontinuities present in traditional designs, preserving the wideband advantage inherent to GRIN media while achieving the desired flat-top pattern.

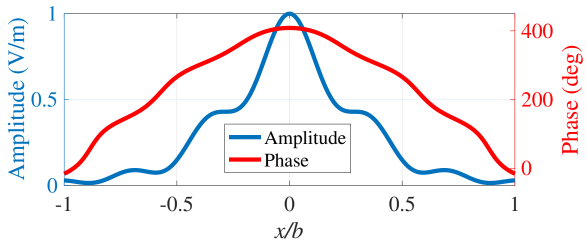

Fig. 7: Amplitude (V/m) (red solid line) and phase (degrees) (blue solid line) of $E_{\mathrm{out}}(x)$, representing the defocalized sinc distribution used to achieve a flat-top beam scanning over the angular range $[-15°, 15°]$. This amplitude and phase profile is employed in the synthesis of the inhomogeneous lens, starting from a rectangular TE_{10} mode.

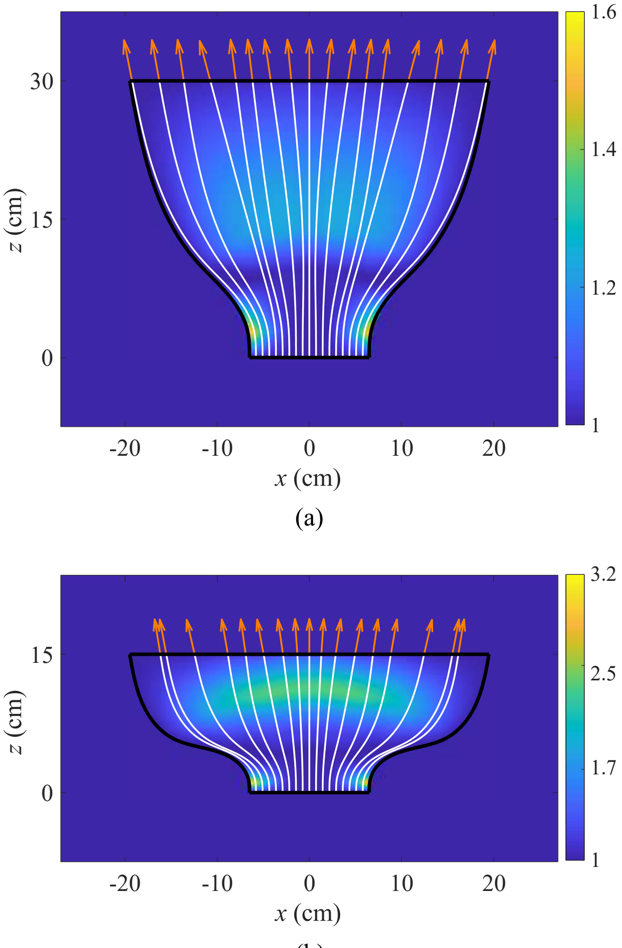

(a)

(b)

Fig. 8: Flat-top beam GRIN lenses: (a) Thick flat-top beam GRIN lens, and (b) thin lens with half the dimensions of (a). The background color represents the refractive index distribution, with the thin lens having twice the maximum permittivity of the thick lens. Rays, shown as white solid lines, are generated using the method from [4].

We consider a PPW with input field given by the fundamental TE_{10} mode

$$E_{\mathrm{in}}(x) \propto \cos\left(\frac{\pi x}{a}\right), \quad |x| \le a/2, \tag{23}$$

where $a = 4.3\lambda_0$ ($\simeq$ 13 cm) at $f_0 = 10$ GHz defines the input aperture width. The target far-field pattern is $\mathcal{P}_{\mathrm{ff}}(\theta) \propto \operatorname{rect}\left(\frac{\theta}{30°}\right)$, corresponding to a rectangular angular spectrum bounded by $k_{x,\max} = k_0 \sin 15°$, where k_0 is the free-space wavenumber. The aperture field at $z_0 = 13\lambda_0$ is computed via inverse fast Fourier transform (IFFT) of the propagated spectrum

$$E_{\mathrm{out}}(x) = \frac{1}{2\pi}\int_{-k_{x,\max}}^{k_{x,\max}} e^{j(k_x x + k_z z_0)}\,dk_x, \quad |x| \le b/2, \tag{24}$$

where $k_z = \sqrt{k_0^2 - k_x^2}$ and $b = 13\lambda_0$ (39 cm) is the output aperture width. This spectral integration introduces the required quadratic phase $\phi_{\mathrm{quad}}(x) = \arg\{E_{\mathrm{out}}\}$ for optimal beam collimation. Fig. 7 shows the normalized amplitude (red solid line) and phase (blue solid line) of the propagated sinc distribution.

To investigate the trade-off between lens thickness and

This article has been accepted for publication in IEEE Transactions on Antennas and Propagation. This is the author's version which has not been fully edited and content may change prior to final publication. Citation information: DOI 10.1109/TAP.2026.3676548

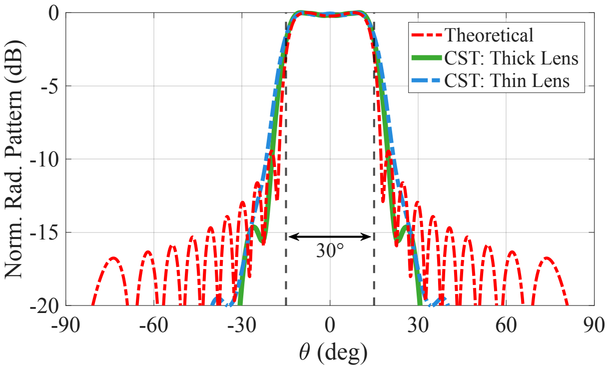

Fig. 9: Flat-top beam normalized radiation pattern distributions (in dB) at $\phi = 0$: theoretical prediction from the FFT of (24) (red dashed line), CST results for the thick lens (green solid line), and CST results for the thin lens (blue dashed line). All results show excellent agreement within the $[-15°, 15°]$ beam formation region.

refractive index contrast, we design two GRIN lens variants using the PTM: a thick lens with thickness $d = 30$ cm and a thin lens with half the thickness, $d = 15$ cm. Fig. 8 illustrates the refractive index distribution of both lenses, with the solid white lines representing the ray trajectories computed using the ray tracing algorithm from [4], and the orange arrows indicating the transmitted rays from the output aperture. As expected, the thin lens exhibits approximately twice the maximum permittivity of the thick lens, demonstrating the expected inverse relationship between thickness and index contrast.

Figure 9 compares the normalized radiation pattern distributions (in dB) at $\phi = 0$: CST results for the thick lens (green solid line), CST results for the thin lens (blue dashed line), and the theoretical IFFT solution of (24) (red dashed line). Excellent agreement among all methods confirms successful flat-top beam formation within $\theta = [-15°, 15°]$ for both lens implementations, validating the PTM's ability to accommodate different design constraints while maintaining performance.

D. Bessel Beam Lens

In the previous examples, we demonstrated the design of GRIN lenses using the PTM, starting from a flat input interface such as the aperture of a rectangular waveguide in a PPW. In this example, we employ a point source positioned at a focal distance F from the lens input aperture to generate a non-diffractive, self-healing Bessel beam in a three-dimensional (3D) configuration.

Bessel beams [37] are a class of non-diffractive solutions to the scalar Helmholtz equation, characterized by a transverse field profile governed by the zeroth-order Bessel function of the first kind

$$E(\rho, z) = E_0 J_0(k_\rho \rho) e^{-j\beta z}, \tag{25}$$

where E_0 is the electric field magnitude, k_ρ is the transverse (radial) wavenumber, $k_0 = 2\pi/\lambda$ is the free-space wavenumber, and $\beta = \sqrt{k_0^2 - k_\rho^2}$ is the longitudinal propagation constant. These beams exhibit two important features:

1) *Non-diffractive propagation*: The beam maintains a localized transverse field distribution over a finite range $z_{\text{max}} = r \cot\theta_a$, called non-diffractive range, where $\theta_a = \arcsin(k_\rho/k_0)$ is the axicon angle and r is the aperture radius.
2) *Self-healing*: The beam reconstructs itself after obstruction, providing robustness in near-field communication and power delivery applications.

These properties make Bessel beams attractive for wireless power transfer, chip-to-chip communication, and near-field links. In response to these use cases, there has been growing interest in generating Bessel beams in recent years, leading to various innovative launcher designs. Notable examples include radial waveguides with metasurfaces [38], [39], leaky wave antennas [40], radial line slot arrays (RLSAs) [41], [42], patch arrays [43], lenses [44], and spline-profile horns [45], [46].

An interesting approach, demonstrated in [47], uses inward-propagating cylindrical waves for the synthesis of the Bessel beam, with the tangential aperture field following a Hankel distribution. Using this approach, in this section, we design a GRIN lens which generates a Bessel beam distribution via Hankel aperture synthesis. The input field of the lens at $z = 0$ is excited by a point source located at $z = -F$ with a normalized pattern equal to $\cos^{4.45}\theta$ and a progression of phase of type $e^{-jk_0 r}$ where $r = \sqrt{\rho^2 + F^2}$, and $\rho \in [0, a]$ spans the lens input aperture of radius a. The target output field at the lens output ($z = d$) is defined using the zeroth-order Hankel function of the first kind

$$E_{\text{out}}(\rho) = E_0^{\text{out}} H_0^{(1)}(k_{\rho a}\rho), \tag{26}$$

where E_0^{out} is the output amplitude, $\rho \in [0, b/2]$ and b is the radius of the output aperture, and $k_\rho = k_0 \sin\theta_a$ is the radial wavenumber, where θ_a is the angle of the axicon, generating a non-diffractive range $z_{\text{max}} = \frac{b}{2}\cot(\theta_a)$.

Under rotational symmetry, the distribution $H_0^{(1)}$ represents inward-propagating conical waves converging toward $\rho = 0$ from all azimuthal directions. Along the optical axis ($\rho = 0$), the interference of these inward Hankel waves produces the Bessel profile $J_0(k_\rho \rho)$. However, since $H_0^{(1)}$ exhibits a singularity at the origin, a spectral filtering step has been applied to remove this non-physical divergence. The removed spectral components correspond to highly evanescent modes, whose contributions decay rapidly and do not influence the observable near-field region. As a result, the filtered field accurately preserves the physical behavior of the beam while eliminating the central singularity. We design our GRIN lens to operate in the Ka-band (26.5–40 GHz) with a central frequency of 33 GHz. The lens dimensions are: focal distance $F = 50$ mm, thickness $d = 100$ mm, input aperture radius $a = 50$ mm, and output aperture radius $b = 100$ mm. The axicon angle is set to $\theta_a = 10°$, resulting in a non-diffractive range $z_{\text{max}} = 280$ mm.

Figure 10(a) illustrates a 2D cross-section of the Bessel beam launcher. The red filled circle represents the point source at $z = -F$, radiating with an amplitude pattern proportional to $\cos^{4.45}(\theta)$. The blue rays show the source radiation incident on the lens at $z = 0$, while the solid white rays inside

This article has been accepted for publication in IEEE Transactions on Antennas and Propagation. This is the author's version which has not been fully edited and content may change prior to final publication. Citation information: DOI 10.1109/TAP.2026.3676548

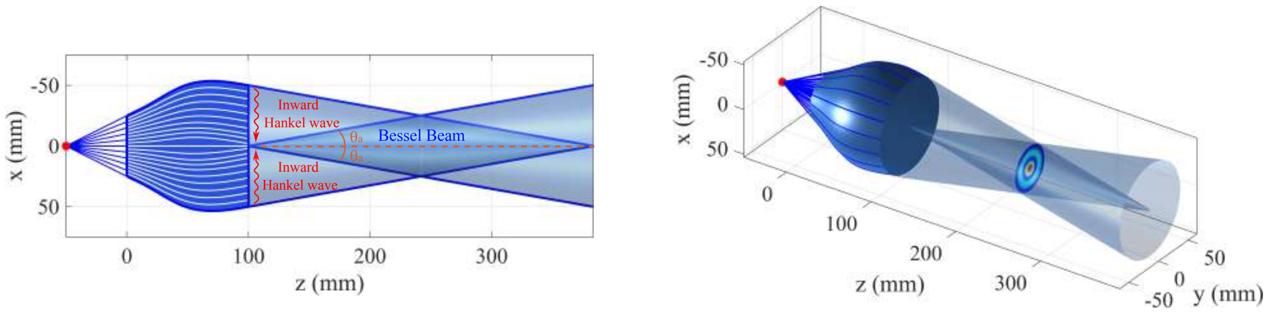

(a) (b)

Fig. 10: Bessel beam launcher configuration: (a) 2D cut in the x-z plane showing the source located at $z = -F$, radiating an amplitude pattern proportional to $\cos^{4.45}(\theta)$ towards the lens. The blue rays represent trajectories from the source impinging on the lens at $z = 0$. Inside the lens, rays (white solid lines) follow clothoid trajectories that transform the incoming wave into the desired Hankel distribution, thus generating the Bessel beam. The output ray direction θ_a corresponds to the axicon angle (here $\theta_a = 10°$), producing a nondiffractive range of approximately 280 mm at the central frequency $f_0 = 33$ GHz. (b) 3D representation of the Bessel beam launcher, with the circle indicating the $J_0(\kappa_\rho \rho)$ Bessel function profile formed.

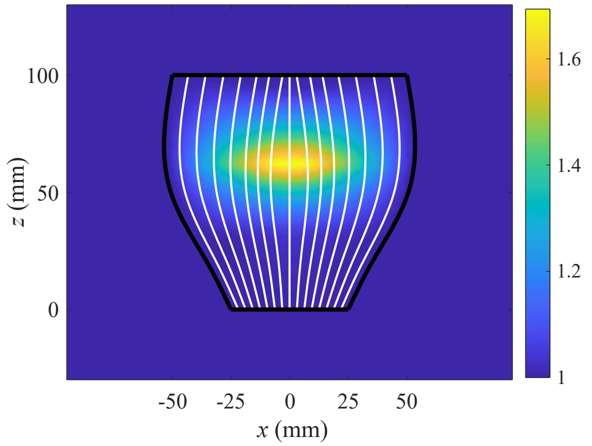

Fig. 11: Bessel beam launcher GRIN lens outlined by its geometry (black solid line), with the background color representing the refractive index distribution, and the white solid lines representing the ray trajectories.

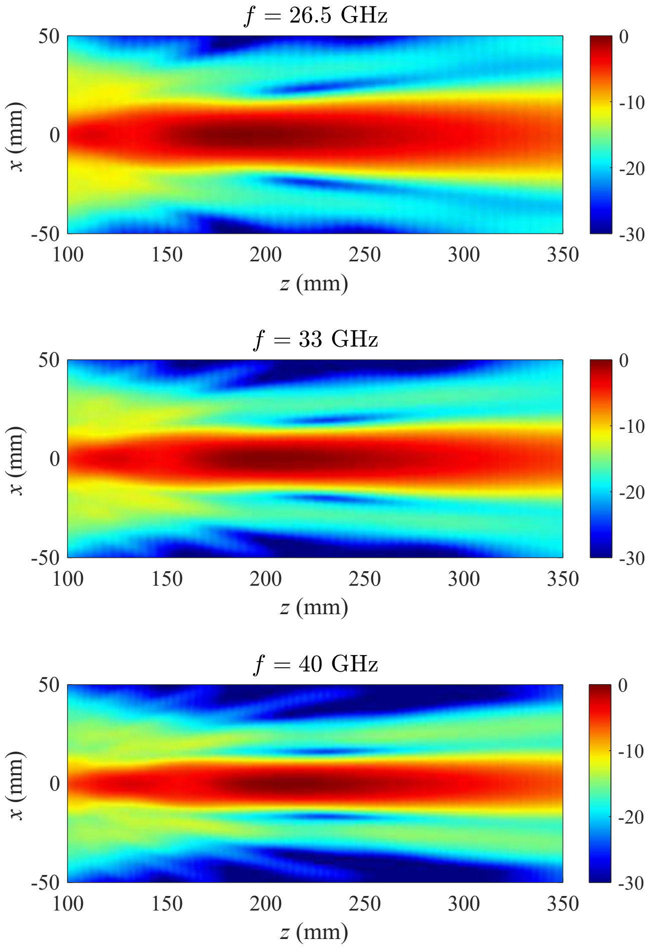

Fig. 12: CST-simulated normalized electric-field magnitude ($|E|$, in dB) in the xoz plane at 26.5, 33, and 40 GHz. The Bessel-beam launcher is designed with an axicon angle of $\theta_0 \approx 10°$, and the corresponding non-diffractive range is approximately 280 mm.

the lens follow clothoid paths, transforming the spherical-shaped wavefront into the desired Hankel distribution. This transformation enables the generation of a Bessel beam over the non-diffractive range $z_{\max}$, with the output ray angle θ_a corresponding to the axicon angle. Fig. 10(b) presents the 3D configuration of the Bessel beam launcher, highlighting the formation of the Bessel profile $J_0(k_\rho \rho)$. After defining the ray trajectories, the PTM was employed to reconstruct the lens refractive index distribution. Fig. 11 shows the resulting refractive index map, with rays overlaid as white solid lines and the lens boundaries outlined in blue. Fig. 12 shows the normalized electric field (in dB) in the x-z plane, obtained from full-wave simulations, spanning from $z = 100$ mm (lens output) to $z = 350$ mm. Fig. 13 presents a cross-section in the x-y plane at $z = 240$ mm, clearly illustrating the formation of the Bessel beam produced by the GRIN lens designed using the PTM. The results are presented for the three operating frequencies: 26.5, 33, and 40 GHz, showing excellent agreement with the expected behavior. Despite the fact that the incident $\cos^{4.45}(\theta)$ pattern was simulated using a rectangular open-ended waveguide, the resulting Bessel beam still exhibits good rotational symmetry. In particular, the central nondiffractive region remains well defined across

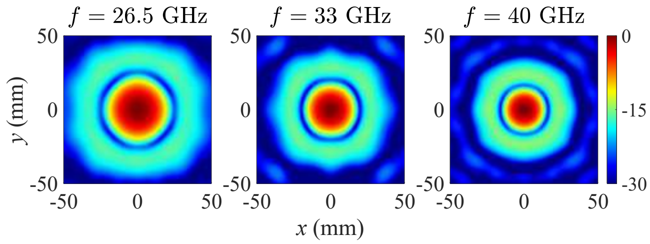

Fig. 13: CST-simulated normalized electric-field magnitude ($|E|$, in dB) cuts in the xoy plane at 26.5, 33, and 40 GHz, evaluated at $z = 140$ mm (half of the non-diffractive range), showcasing the formation of the Bessel profile $J_0(\kappa_\rho \rho)$ corresponding to an axicon angle of $10°$.

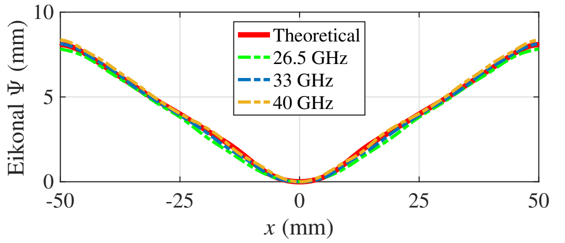

Fig. 14: Eikonal distribution Ψ (in mm) at the lens aperture for the generated Hankel beam. Theoretical design at the central frequency (red solid line) is compared with CST simulations at 26.5 GHz (green dashed), 33 GHz (blue dashed), and 40 GHz (orange dashed).

all frequencies, confirming the effectiveness of the lens design.

Despite the fact that the incident $\cos^{4.45}(\theta)$ pattern was simulated using a rectangular open-ended waveguide, the resulting Bessel beam still exhibits good rotational symmetry. In particular, the central nondiffractive region remains well defined across all frequencies. Fig. 14 shows the eikonal distribution Ψ (in mm) at the lens aperture for the generated Hankel beam. The theoretical eikonal, computed at the central design frequency, is compared with CST simulation results at the three operating frequencies. The eikonal is essentially identical across all frequencies, demonstrating the broadband and frequency-stable behavior of the lens. This confirms that the lens preserves the designed phase distribution at the aperture, ensuring consistent Hankel beam generation over the operating band, a key advantage of GRIN-lens antenna designs.

Table I compares the theoretical first null of the $J_0(k_\rho \rho)$ Bessel function with the corresponding values obtained from simulations at the three frequencies, evaluated in three planes: $\phi = 0°$ (E-plane), $\phi = 45°$, and $\phi = 90°$ (H-plane). The results show very good agreement across all frequencies and planes.

TABLE I: Comparison of theoretical and simulated first null positions (in mm) of $J_0(\kappa_\rho \rho)$ in different planes.

	Theoretical	**Simulation**		
	$\phi \in [0°, 360°]$	$\phi = 0°$ (E-plane)	$\phi = 45°$	$\phi = 90°$ (H-plane)
26.5 GHz	24.95	25.21	24.75	25.81
33 GHz	20.04	20.0	20.37	20.2
40 GHz	16.53	16.2	16.41	16.60

E. Transformation of Rectangular TE$_{10}$ Mode to Uniform Circular Aperture

As a final example, we apply the PTM to transform the field of a fundamental TE$_{10}$ mode in a rectangular waveguide into a uniform distribution over a circular aperture. This task is particularly challenging due to the geometric transition from a rectangle to a circle. To address this, the PTM is applied along multiple angular cuts, ensuring local power conservation while preserving the polarization of the incident field. The design carefully maps the rectangular input onto the circular output, accounting for both azimuthal and radial variations, making the system inherently three-dimensional and non-trivial to synthesize.

The normalized input power density for the TE$_{10}$ mode on a rectangular aperture of dimensions $a \times b$ in cylindrical is given by

$$I_{\text{in}}(\rho, \phi) = \frac{2}{ab} \cos^2\left(\frac{\pi \rho \cos\phi}{a}\right), \tag{27}$$

where the maximum radial extent at a given angle ϕ is $\rho_{\max,i}(\phi) = \min\left(\frac{a}{2|\cos\phi|}, \frac{b}{2|\sin\phi|}\right)$. This angle-dependent boundary accounts for the rectangular shape of the input aperture and defines the spatial limits of the TE$_{10}$ field. The input field is thus non-uniform and varies along both the radial and azimuthal directions. For the output, our objective is to transform this distribution into a uniform power density over a circular aperture of radius R, $I_{\text{out}}(\rho', \phi') = \frac{1}{\pi R^2}$, with a fixed maximum output radius $\rho_{\max,o} = R$. Achieving this transformation requires careful redistribution of energy from the rectangular input to the circular output while preserving total power and phase continuity. This sets the stage for applying the PTM along selected angular cuts, allowing a smooth and physically realizable mapping between the two geometries. The mapping between the input and output azimuthal angles, $\phi \Leftrightarrow \phi'$, is determined by enforcing power conservation

$$\begin{aligned}\int_0^{\phi} \int_0^{\rho_{\max,i}(\varphi)} I_{\text{in}}(\rho, \varphi)\, \rho\, d\rho\, d\varphi = \\ \int_0^{\phi'} \int_0^{\rho'_{\max,o}(\varphi')} I_{\text{out}}(\rho', \varphi')\, \rho'\, d\rho'\, d\varphi'.\end{aligned} \tag{28}$$

For the specific case of transforming a rectangular TE$_{10}$ aperture of size $a \times b$ to a circular aperture of radius R, this relation reduces to

$$\begin{aligned}\int_0^{\phi} \left[\int_0^{\rho_{\max,i}(\varphi)} \frac{2}{ab} \cos^2\left(\frac{\pi \rho \cos\varphi}{a}\right) \rho\, d\rho\right] d\varphi = \\ = f_i(\phi) = \frac{\phi'}{2\pi} = f_o(\phi'),\end{aligned} \tag{29}$$

which defines the mapping between input and output angles. Equivalently, the mapping can be expressed as $\phi = f_i^{-1}[f_o(\phi')]$ or $\phi' = f_o^{-1}[f_i(\phi)]$. This procedure ensures that the cumulative power up to angle ϕ in the rectangular input is matched to the cumulative power up to angle ϕ' in the circular output, preserving total energy during the transformation.

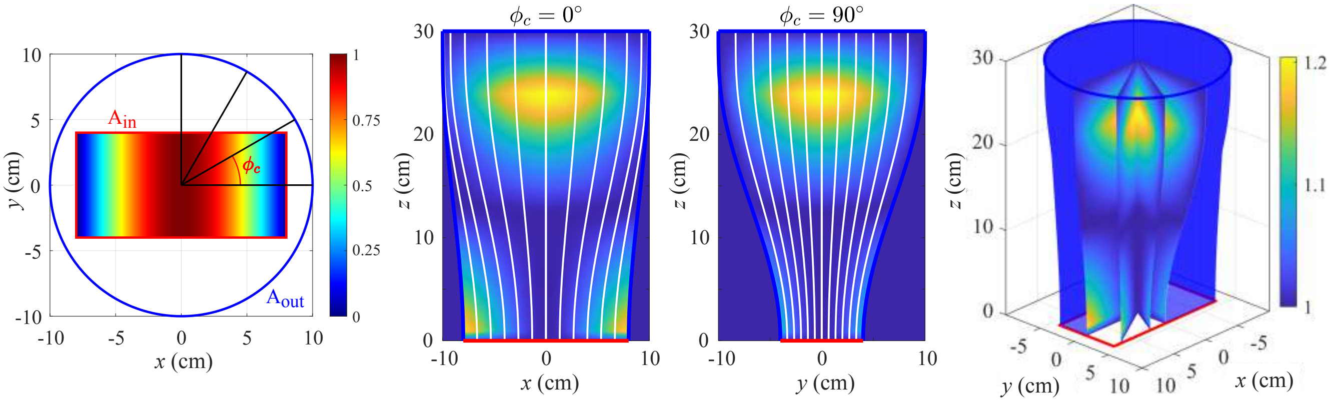

(a) (b) (c) (d)

Fig. 15: Three-dimensional GRIN lens design transforming a rectangular TE_{10} input aperture into a circular output aperture. (a) Input (A_{in}, red solid line) and output (A_{out}, blue solid line) regions in the x–y plane, with four angular cuts at $\phi_c = 0°, 30°, 60°, 90°$ where the PTM is applied to enforce power conservation. The background shows the amplitude of the TE_{10} mode in dB. (b) Refractive index distribution and ray trajectories in the x–z plane ($\phi_c = 0°$). (c) Refractive index distribution and ray trajectories in the y–z plane ($\phi_c = 90°$). (d) Three-dimensional view of the GRIN lens showing the four cuts of the refractive index profile.

Due to the rotational symmetry of the circular output, the azimuthal coordinate is preserved ($\phi' = \phi$). However, a ϕ-dependent radial mapping is required to account for the geometric asymmetry between the rectangular input and the circular output. This radial mapping, $\rho \leftrightarrow \rho'$, is established by enforcing local power conservation within differential ray tubes, by means of the implicit definition

$$\begin{aligned}\frac{\int_0^{\rho} I_{\mathrm{in}}(\sigma,\phi)\,\sigma\,d\sigma}{\int_0^{\rho_{\max,i}(\phi)} I_{\mathrm{in}}(\sigma,\phi)\,\sigma\,d\sigma} &= g_i(\rho) = \\ = \frac{\int_0^{\rho'} I_{\mathrm{out}}(\sigma',\phi)\,\sigma'\,d\sigma'}{\int_0^{\rho_{\max,o}} I_{\mathrm{out}}(\sigma',\phi)\,\sigma'\,d\sigma'} &= g_o(\rho'),\end{aligned} \tag{30}$$

which defines the relationship between input and output radii. Equivalently, the mapping can be expressed as $\rho = g_i^{-1}[g_o(\rho')]$ or $\rho' = g_o^{-1}[g_i(\rho)]$. This ensures that the fractional power enclosed within a given input radius ρ is matched exactly to the corresponding fractional power within the output radius ρ', thereby preserving the local power density and achieving a physically realizable transformation from the rectangular TE_{10} field to a uniform circular distribution. For this example, we consider an input aperture of dimensions $a = 16$ cm and $b = 8$ cm, an output aperture with radius $R = 10$ cm, and a lens thickness of $d = 30$ cm, at the operating frequency $f_0 = 10$ GHz. Fig. 15(a) illustrates the x–y plane of the lens configuration: the input TE_{10} field (in V/m) is shown within the input region A_{in}, delimited by the red solid line, while the output region A_{out} is bounded by the blue solid line corresponding to a circle of radius R. Four angular cuts at $\phi_c = \{0°, 30°, 60°, 90°\}$ are shown for illustration. The PTM is applied along the cuts to ensure power conservation, as expressed in (30). Figures 15(b) and 15(c) show the refractive index distribution of the GRIN lens together with the corresponding ray trajectories (depicted as white solid lines) for the cuts at $\phi_c = 0°$ (x–z plane) and $\phi_c = 90°$ (y–z plane), respectively. Finally, Fig. 15(d) presents the three-dimensional view of the GRIN lens, including the four cuts where the refractive index distribution is displayed. The cuts and the number of rays shown are only for illustration purposes; in the actual synthesis process, a larger number of cuts and rays were employed.

Fig. 16 depicts two cuts of the real part of the electric field, $\Re\{\mathbf{E}\}$ (in dB), at $\phi_c = 0°$ and $\phi_c = 90°$. In both cuts, a plane wave is clearly generated at the output, with power spreading as expected. For $\phi_c = 90°$, some power is observed close to the input due to the high field intensity along the y-axis of the TE_{10} mode, as depicted in Fig. 15(a). This behavior is reasonable and expected, since spillover effects naturally occur when a strong guided field transitions to free space and cannot be entirely eliminated near the aperture edges. Finally, Fig. 17 compares the gain (in dBi) between the CST-simulated GRIN lens at 10 GHz (green solid line) and the theoretical gain of a uniform circular aperture of radius $a = 10$ cm (red dashed line), whose theoretical gain is 26.42 dBi. The excellent

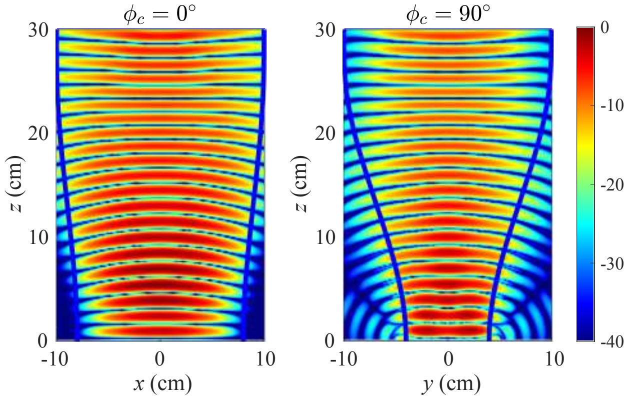

(a) (b)

Fig. 16: Two cuts of the real part of the electric field, $\Re\{\mathbf{E}\}$ (in dB) at $\phi_c = 0°$ and $90°$ (from left to right). A plane wave is generated at the output in all cuts, with some power appearing near the input for 90° due to spillover effects from the TE_{10} mode.

This article has been accepted for publication in IEEE Transactions on Antennas and Propagation. This is the author's version which has not been fully edited and content may change prior to final publication. Citation information: DOI 10.1109/TAP.2026.3676548

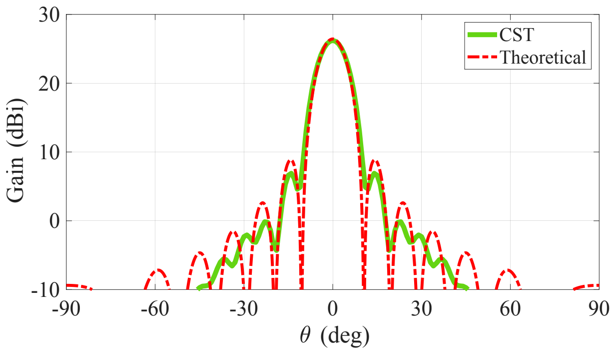

Fig. 17: Comparison of the gain (in dBi) at $\phi = 0$ between the CST-simulated (green solid line) GRIN lens at 10 GHz and the theoretical gain (red dashed line) of a uniform circular aperture of radius 10 cm, whose maximum directivity is 26.42 dBi. The agreement between the two curves is excellent, demonstrating that the GRIN lens effectively forms an equivalent uniform circular aperture, starting from a rectangular TE_{10} mode.

agreement between the curves demonstrates that the GRIN lens effectively forms an equivalent uniform circular aperture, starting from a rectangular TE_{10} mode.

IV. CONCLUSIONS

The core theoretical contribution of PTM is the establishment of explicit relationships linking ray curvature, phase progression, and refractive-index gradients, which enables closed-form expressions for spatially varying dielectric profiles. Its analytical nature allows designers to choose ray paths that reduce fabrication complexity, with clothoid trajectories identified as an optimal solution because their linearly varying curvature produces smooth, bounded refractive-index gradients.

Comprehensive validation through five distinct design examples demonstrates the method's versatility and rigor:

- The exact analytical retrieval of the Maxwell Fish-Eye lens profile confirms the theoretical foundation and mathematical consistency of the PTM formulation.
- The telescopic GRIN lens design achieves precise 2× aperture magnification with corresponding 3 dB gain enhancement, validating amplitude and phase control capabilities.
- The flat-top beam generator successfully transforms a rectangular waveguide mode into uniform ±15° angular coverage, demonstrating complex field transformation capabilities.
- The Bessel beam launcher produces extended non-diffractive propagation through Hankel aperture synthesis, showcasing near-field manipulation potential.
- The 3D transformation from rectangular TE_{10} mode to uniform circular aperture distribution illustrates the method's applicability to geometrically complex scenarios.

These examples demonstrate the ability to address scenarios that are notoriously difficult to treat with conventional GRIN synthesis methods, that would typically require extensive numerical optimization, cases that indeed are handled analytically by PTM. Full-wave simulations and geometrical optics analysis consistently validate the designs, showing excellent agreement with theoretical predictions across multiple frequency bands. The PTM establishes a new paradigm for GRIN lens design that unites analytical exactness with practical manufacturability, offering significant advantages for microwave and millimeter-wave applications where bandwidth, efficiency, and fabrication constraints are critical. The method's direct synthesis approach eliminates iterative optimization while providing physical insight into the relationship between ray trajectories and material properties, making it a powerful tool for next-generation antenna systems.

REFERENCES

[1] M. Born and E. Wolf, *Principles of optics*. Cambridge University Press, 1999.

[2] L. B. Felsen and N. Marcuvitz, *Radiation and Scattering of Waves*. IEEE Press series on Electromagnetic Wave Theory, 1994.

[3] Y. A. Kravtsov and Y. I. Orlov, *Geometrical Optics of Inhomogeneous Media*. Springer Series on Wave Phenomena, Springer-Verlag Berlin Heidelberg, 1990.

[4] I. Gashi, A. Paraskevopoulos, S. Maci, and M. Albani, "Go analysis of grin lens antennas by combining in a single ode, field and wavefront-curvature transport to the ray tracing," *IEEE Transactions on Antennas and Propagation*, vol. 72, no. 3, pp. 2147–2160, 2024.

[5] I. Gashi, S. Maci, and M. Albani, "Numerical solution of the eikonal and transport equations for grin lens antennas by using the lax–friedrichs sweeping method," *IEEE Transactions on Antennas and Propagation*, vol. 73, no. 9, pp. 6686–6696, 2025.

[6] S. Zhang, R. K. Arya, S. Pandey, Y. Vardaxoglou, W. Whittow, and R. Mittra, "3d-printed planar graded index lenses," *IET Microwaves, Antennas & Propagation*, vol. 10, no. 13, pp. 1411–1419, 2016.

[7] A. Papathanasopoulos, J. Budhu, Y. Rahmat-Samii, R. E. Hodges, and D. F. Ruffatto, "3-d-printed shaped and material-optimized lenses for next-generation spaceborne wind scatterometer weather radars," *IEEE Transactions on Antennas and Propagation*, vol. 70, no. 5, pp. 3163–3172, 2022.

[8] A. Paraskevopoulos, F. Maggiorelli, I. Gashi, C. D. Giovampaola, M. Albani, and S. Maci, "3-d printed all-dielectric grin lens antenna with an integrated feeder," *IEEE Open Journal of Antennas and Propagation*, vol. 4, pp. 528–536, 2023.

[9] N. Kundtz and D. R. Smith, "Extreme-angle broadband metamaterial lens," *Nature Materials*, vol. 9, pp. 129–132, 2010.

[10] Y. Yang, R. Wang, Y. Hao, and Z. Li, "A 3-d luneburg lens antenna fabricated by graded dielectric metamaterials," *IEEE Transactions on Antennas and Propagation*, vol. 64, no. 6, pp. 2446–2455, 2016.

[11] R. K. Luneburg, *Mathematical Theory of Optics*. Brown University Press, 1944.

[12] J. Maxwell, "Solution of problems. prob. 3, vol. viii, p.118," *The Cambridge and Dublin Mathematical Journal*, vol. IX, pp. 9–11, February 1854.

[13] Z. Li, X. Shen, Y. Liu, and Y. Hao, "Flat luneburg lens via transformation optics," *IEEE Transactions on Antennas and Propagation*, vol. 61, no. 6, pp. 3109–3114, 2013.

[14] M. Budhu and Y. Rahmat-Samii, "Inhomogeneous dielectric lens design based on curved-ray go and pso," *IEEE Transactions on Antennas and Propagation*, vol. 67, no. 6, pp. 3657–3669, 2019.

[15] H. Eskandari, M. Shokooh-Saremi, and T. Tyc, "Graded index all-dielectric lens antenna designed by phase manipulation and optical path rescaling," *Optics Laser Technology*, vol. 161, p. 109125, 2023.

[16] E. B. Whiting, S. D. Campbell, G. Mackertich-Sengerdy, S. Soltani, D. H. Werner, and P. L. Werner, "Adjoint optimization of 3d printed rf grin lenses," in *2022 16th European Conference on Antennas and Propagation (EuCAP)*, 2022, pp. 1–3.

[17] E. B. Whiting, G. Mackertich-Sengerdy, S. D. Campbell, S. Soltani, M. P. Haack, J. P. Barrett, J. W. Withrow, J. A. Bossard, and D. H. Werner, "Adjoint sensitivity optimization of three-dimensional directivity-enhancing, size-reducing grin lenses," *IEEE Antennas and Wireless Propagation Letters*, vol. 21, no. 11, pp. 2166–2170, 2022.

[18] J. Stoer, "Curve fitting with clothoidal splines," *Journal of Research of the National Bureau of Standards*, vol. 87, no. 4, pp. 317–346, 1982.

This article has been accepted for publication in IEEE Transactions on Antennas and Propagation. This is the author's version which has not been fully edited and content may change prior to final publication. Citation information: DOI 10.1109/TAP.2026.3676548

[19] E. Bertolazzi and M. Frego, "On the g2 hermite interpolation problem with clothoids," *Journal of Computational and Applied Mathematics*, vol. 341, pp. 99–116, 2018.

[20] E. Bertolazzi, "ebertolazzi/clothoids," https://github.com/ebertolazzi/Clothoids, 2026, gitHub repository, accessed February 26, 2026.

[21] A. J. Ward and J. B. Pendry, "Refraction and geometry in maxwell's equations," *Journal of Modern Optics*, vol. 43, no. 4, pp. 773–793, 1996.

[22] H. Chen, C. T. Chan, and P. Sheng, "Transformation optics and metamaterials," *Nature Materials*, vol. 9, pp. 387–396, 2010.

[23] J. E. Eaton, "On spherically symmetric lenses," *IRE Transactions on Antennas and Propagation*, vol. 4, pp. 66–71, 1952.

[24] Nemoto, S. and Makimoto, T., "Refractive-index distribution for a prescribed ray path," *J. Opt. Soc. Am. B*, vol. 69, no. 3, pp. 450–454, 1979.

[25] Miñano, J. C., "Refractive-index distribution in two-dimensional geometry for a given one-parameter manifold of rays," *J. Opt. Soc. Am. A*, vol. 2, no. 11, pp. 1821–1825, 1985.

[26] Lin, D. and Teichman, J. and Leger, J. R., "Deflectometry for measuring inhomogeneous refractive index fields in two-dimensional gradient-index elements," *Journal of the Optical Society of America A*, vol. 32, no. 5, p. 991, 2015.

[27] Gómez-Correa, J. E. and others, "Symmetric gradient-index media reconstruction," *Opt. Express*, vol. 31, no. 18, p. 29196, 2023.

[28] Borghero, F. and Demontis, F., "Three-dimensional inverse problem of geometrical optics: a mathematical comparison between Fermat's principle and the eikonal equation," *J. Opt. Soc. Am. A*, vol. 33, no. 9, pp. 1710–1722, 2016.

[29] A. Mikš and P. Novák, "Theoretical and experimental analysis of basic parameters of two-element optical systems," *Applied Optics*, vol. 51, no. 30, pp. 7286–7294, 2012.

[30] G. Galilei, *Sidereus Nuncius*. Venice: Thomas Baglioni, 1610, first publication describing Galileo's refracting telescope.

[31] A. Paraskevopoulos, I. Gashi, M. Albani, and S. Maci, "Analytical formulas for refractive indices of a telescopic grin lens for aperture magnification," *IEEE Antennas and Wireless Propagation Letters*, vol. 21, no. 11, pp. 2206–2210, 2022.

[32] N. T. Nguyen, R. Sauleau, and L. L. Coq, "Reduced-size double-shell lens antenna with flat-top radiation pattern for indoor communications at millimeter waves," *IEEE Transactions on Antennas and Propagation*, vol. 59, no. 6, pp. 2424–2429, Jun 2011.

[33] A. K. Singh, M. P. Abegaonkar, and S. K. Koul, "Wide angle beam steerable high gain flat top beam antenna using graded index metasurface lens," *IEEE Transactions on Antennas and Propagation*, vol. 67, no. 10, pp. 6334–6343, Oct 2019.

[34] H. Wang, Z. Zhang, and Z. Feng, "A beam-switching antenna array with shaped radiation patterns," *IEEE Antennas and Wireless Propagation Letters*, vol. 11, pp. 818–821, 2012.

[35] X. Yang and X. Liu, "Design of a wide-beam microstrip array antenna for automotive radar application," *IEEE Access*, vol. 9, pp. 142 340–142 347, 2021.

[36] N. Castro and E. Rajo-Iglesias, "Array of stacked groove gap waveguide leaky wave antennas for the synthesis of a broad-beam radiation pattern," *IEEE Transactions on Antennas and Propagation*, vol. 73, no. 3, pp. 1515–1522, 2025.

[37] J. Durnin, J. J. Miceli, and J. H. Eberly, "Diffraction-free beams," *Phys. Rev. Lett.*, vol. 58, pp. 1499–1501, Apr 1987.

[38] M. Ettorre and A. Grbic, "Generation of propagating Bessel beams using leaky-wave modes," *IEEE Trans. Antennas Propag.*, vol. 60, no. 8, pp. 3605–3613, 2012.

[39] W. Fuscaldo, G. Valerio, A. Galli, R. Sauleau, A. Grbic, and M. Ettorre, "Higher-order leaky-mode Bessel-beam launcher," *IEEE Trans. Antennas Propag.*, vol. 64, no. 3, pp. 904–913, 2016.

[40] E. Negri, F. Giusti, W. Fuscaldo, P. Burghignoli, E. Martini, and A. Galli, "Ultra-long-range bessel beams via leaky waves with mitigated open stopband," *Applied Physics Letters*, vol. 126, no. 12, p. 121703, 03 2025.

[41] A. Mazzinghi, M. Balma, D. Devona, G. Guarnieri, G. Mauriello, M. Albani, and A. Freni, "Large depth of field pseudo-Bessel beam generation with a RLSA antenna," *IEEE Trans. Antennas Propag.*, vol. 62, no. 8, pp. 3911–3919, 2014.

[42] S. C. Pavone, M. Ettorre, M. Casaletti, and M. Albani, "Analysis and design of Bessel beam launchers: Transverse polarization," *IEEE Trans. Antennas Propag.*, vol. 69, no. 8, pp. 5175–5180, 2021.

[43] P. Lemaitre-Auger, S. Abielmona, and C. Caloz, "Generation of Bessel beams by two-dimensional antenna arrays using sub-sampled distributions," *IEEE Trans. Antennas Propag.*, vol. 61, no. 4, pp. 1838–1849, 2013.

[44] N. Chiotellis, S. Zhang, Y. C. Vardaxoglou, and A. Grbic, "X wave radiator implemented with 3-D printed metamaterials," *IEEE Trans. Antennas Propag.*, vol. 68, no. 7, pp. 5478–5486, 2020.

[45] S. Paković, N. Bartolomei, M. J. Mencagli, M. Ettorre, R. Sauleau, and D. González-Ovejero, "A fast and accurate method of synthesizing X-wave launchers by metallic horns," *IEEE Access*, vol. 9, pp. 1996–2006, 2021.

[46] J. Taillieu, J. Pascual, S. Paković, X. Morvan, W. Fuscaldo, M. Ettorre, and D. González-Ovejero, "High-data-rate and resilient wireless links at the w-band enabled by all-metal spline horns," *IEEE Transactions on Antennas and Propagation*, vol. 73, no. 3, pp. 1834–1839, 2025.

[47] M. Albani, S. C. Pavone, M. Casaletti, and M. Ettorre, "Generation of non-diffractive bessel beams by inward cylindrical traveling wave aperture distributions," *Opt. Express*, vol. 22, no. 15, pp. 18 354–18 364, Jul 2014.

Ilir Gashi (Member, IEEE) was born in Prizren, Kosovo, in 1996. He received his Laurea Degree (Cum Laude) in Electronics and Communications Engineering from the University of Siena, Italy, in 2021, and completed his Ph.D. at the same institution in 2025. He is currently a Postdoctoral Researcher at the University of Siena, where his research focuses on the analysis and design of inhomogeneous lens antennas and the modeling of reconfigurable intelligent surfaces (RIS). He was the recipient of the 2022 IEEE AP-S Doctoral Research Grant, the 2023 C. J. Reddy Travel Grant, the 2023 IEEE AP-S Fellowship Award, an Honorable Mention in the Student Paper Competition at the IEEE AP-S/URSI 2024 Conference, and the Young Scientist Award at URSI EMTS 2025.

Stefano Maci (Fellow, IEEE) received the Laurea degree (cum laude) from the University of Florence, Florence, Italy, in 1987. He was a co-founder of six spin-off companies. Since 1997, he has been a Professor with the University of Siena, Siena, Italy. In 2004, he was the Founder of the European School of Antennas (ESoA), a postgraduate school that presently comprises 34 courses on antennas, propagation, electromagnetic theory, and computational electromagnetics, and 150 teachers coming from 15 countries. Since 2004, he has been the Director of ESoA. From 2008 to 2015, he was the Director of the Ph.D. program in information engineering and mathematics with the University of Siena. His research activity is documented in 200 papers published in international journals (among which 100 on IEEE journals), 14 book chapters, and about 600 papers in proceedings of international conferences. His research interests include high-frequency and beam representation methods, computational electromagnetics, large phased arrays, planar antennas, reflector antennas and feeds, metamaterials, and metasurfaces. Prof. Maci was a member of the AdCom of IEEE Antennas and Propagation Society (AP-S), the Board of Directors of the European Association on Antennas and Propagation (EurAAP), and the Antennas and Propagation Executive Board of the Institution of Engineering and Technology (IET), U.K. From 2013 to 2015, he was a member of the first National Italian Committee for Qualification to Professor. Since 2000, he has been a member of the Technical Advisory Board of 16 international conferences and the Review Board of six international journals. He was a recipient of the EurAAP Award in 2014, the IEEE Schelkunoff Transaction Prize in 2016, the Chen-To Tai Distinguished Educator Award in 2016, and the URSI Dellinger Gold Medal in 2020. He was the Chair of the Award Committee of IEEE AP-S. He has been the Technical Program Committee (TPC) Chair of the METAMATERIAL 2020 Conference and the General Chairperson of the European Conference on Antennas and Propagation (EuCAP) 2023. From 2004 to 2007, he was a Work Package (WP) Leader of the Antenna Center of Excellence (ACE; FP6-EU), and from 2007 to 2010, he was an International Coordinator of the 24-Institution Consortium of a Marie Curie Action (FP6). He founded and was the Director of the consortium FORESEEN, involving 48 European (EU) institutions. He was a Principal Investigator of the Future Emerging Technology Project “Nanoarchitectronics” of the 8th EU Framework Program. He is a Principal Investigator of the EU Program “Metamask.” Since 2010, he has been a principal investigator of six cooperative projects and a university coordinator of about other 20 cooperative projects financed by the European Space Agency. He has been a Distinguished Lecturer of the IEEE AP-S. He has been an EuRAAP Distinguished Lecturer of the Ambassador Program. In the last ten years, he has been invited 25 times as a keynote speaker in international conferences. He was the President of the IEEE Antennas and Propagation Society 2023. He was an Associate Editor of the IEEE Transactions on Antennas and Propagation.

Matteo Albani (Fellow, IEEE) received the Laurea degree in electronic engineering and the Ph.D. degree in telecommunications engineering from the University of Florence, Florence, Italy, in 1994 and 1999, respectively. From 2001 to 2005, he was an Assistant Professor with the University of Messina, Messina, Italy. He is currently a Full Professor with the Information Engineering and Mathematics Department, University of Siena, Siena, Italy, where he is the Director of the Applied Electromagnetics Laboratory. He has authored or coauthored more than 80 journal articles and more than 200 conference papers. His research interests are in the areas of high-frequency methods for electromagnetic scattering and propagation, numerical methods for array antennas, antenna analysis, and design, metamaterials. Dr. Albani is a member of EurAAP, URSI, and SiEM. He was a recipient of the Best Paper Awards at the XIV RiNEM 2002, the URSI EMTS 2004, the European AMTA Symposium 2006, the URSI EMTS 2010, the EuCAP 2014, and the EuCAP 2018.